SCIENTIFIC REPORTS

OPEN

Synthesis of α-Fe_2O_3/Bi_2WO_6 layered heterojunctions by *in situ* growth strategy with enhanced visible-light photocatalytic activity

Received: 26 February 2019
Accepted: 30 April 2019
Published online: 17 May 2019

Taiping Xie[1], Yue Liu[1], Haiqiang Wang[1] & Zhongbiao Wu[1,2]

Layered heterojunction structure with larger interface region for electron migration has attracted much attention in recent years. In this work, layered α-Fe_2O_3/Bi_2WO_6 heterojunctions with strong interlayer interaction were successfully synthesized through a facile *in situ* growth method. The strong interaction between α-Fe_2O_3 and Bi_2WO_6 had resulted in excellent photoelectrochemical performance. It was found that such structure promoted the interfacial photogenerated charges separation according to EIS and Tafel analysis, except for the expansion of visible-light absorption range. PL and TRPL characterizations further demonstrated that the recombination ratio of photoexcited electron-hole pairs was greatly reduced. The toluene photocatalytic degradation tests had showed that α-Fe_2O_3/Bi_2WO_6 composites exhibited much well activity under visible-light irradiation. Especially, 4%-Fe_2O_3/Bi_2WO_6 sample displayed the highest photocatalytic activity, which was around 3 and 4 times higher than that of pure Bi_2WO_6 and α-Fe_2O_3. Based on ESR results and free radical trapping experiments, hydroxyl radicals (·OH) and holes (h^+) were regarded as the main active species. The establishment of Fe_2O_3/Bi_2WO_6 with layered heterojunctions could provide new insights into the construction of novel photocatalysts.

In recent years, indoor air pollution caused by volatile organic pollutants (VOCs) has attracted lots of public attentions. Photocatalytic oxidation was considered as an environmental-friendly technology for indoor VOCs purification[1–6]. Therefore, many kinds of photocatalysts have been extensively investigated, such as TiO_2[7–9], ZnO[10,11], SnO_2[12], $SrTiO_3$[13] and so on. However, these semiconductors still have some common shortcomings, such as narrow light absorption range and high recombination ratio of photogenerated charges[14]. Thus, developing visible-light driven and highly active photocatalysts is one of the most urgent topics.

N-type Bi_2WO_6 has widely regarded as a promising photocatalyst for its outstanding photooxidation ability, nontoxicity, well thermal and chemical stability[15,16]. Nevertheless, pure Bi_2WO_6 can't efficaciously utilize visible light due to the fact that it can only be driven by light shorter than 450 nm[17,18]. Moreover, low separation ratio of photogenerated electrons and holes also impedes its application. Semiconductor heterojunction has been demonstrated to be an effective way to solve this issue above, such as the coupling of MoS_2/Bi_2WO_6[19], g-C_3N_4/Bi_2WO_6[20], CeO_2/Bi_2WO_6[21], BiOBr/Bi_2WO_6[22] and so on.

Layered heterojunction photocatalyst possesses larger interfacial area compared to line contact and point contact heterojunction photocatalysts, which benefits the transfer of photogenerated electron-hole pairs[23]. By taking this advantage into consideration, many photocatalysts with layered heterostructure have been fabricated, such as SnS_2/g-C_3N_4[23], g-C_3N_4/Bi_2WO_6[24], g-C_3N_4/$Bi_{20}TiO_{32}$[25], α-Fe_2O_3/graphene[26] and so on. Motivated by the above work, Bi_2WO_6 coupled with α-Fe_2O_3 (a low-price and narrow band gap semiconductor) nanosheets as layered heterojunction photocatalyst may exhibit significantly enhanced photoinduced interfacial charge transfer rate, which could effectively promote the photocatalytic activity.

In this work, layered α-Fe_2O_3/Bi_2WO_6 heterojunctions were fabricated via a facile *in situ* growth hydrothermal method. And toluene was chosen as a typical kind of indoor VOCs in the experiment. Then, the

[1]Key Laboratory of Environment Remediation and Ecological Health, Ministry of Education, Department of Environmental Engineering, Zhejiang University, 866 Yuhangtang Road, Hangzhou, 310058, P.R. China. [2]Zhejiang Provincial Engineering Research Center of Industrial Boiler & Furnace Flue Gas Pollution Control, 866 Yuhangtang Road, Hangzhou, 310058, P.R. China. Correspondence and requests for materials should be addressed to Y.L. (email: yueliu@zju.edu.cn)

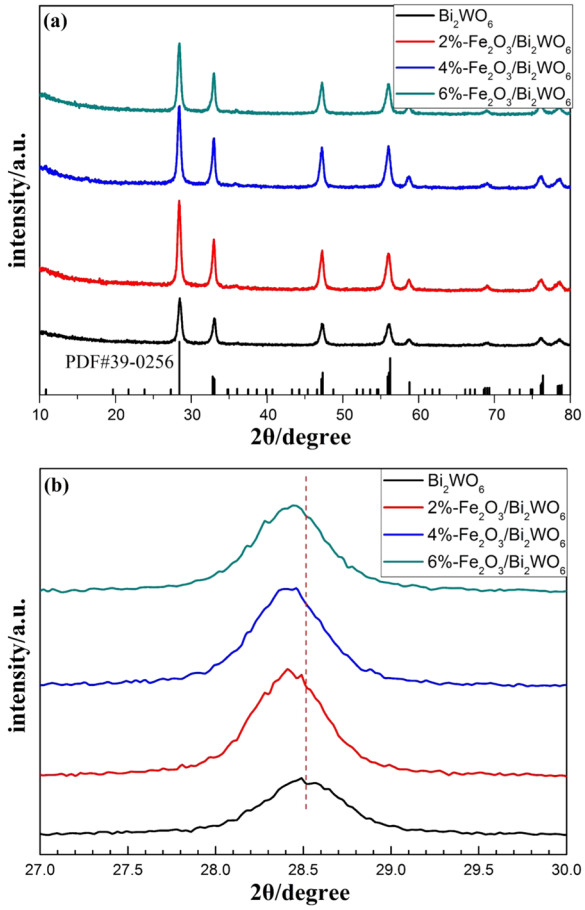

Figure 1. (**a**) XRD patterns of pure Bi_2WO_6 and Fe_2O_3/Bi_2WO_6 composites. (**b**) Enlargement of XRD peaks in lattice (131) plane.

photodegradation efficiency of gaseous toluene under visible light irradiation was tested. After that, the inherent structure-performance relationship was then disclosed based on the physiochemical and photo-electrochemical characterizations. The main purpose of our work was to shed new light on the synthesis of layered heterojunctions and reveal the role of such structure in photocatalytic process.

Experimental

Chemicals. $Bi(NO_3)_3{\cdot}5H_2O$, $Na_2WO_4{\cdot}2H_2O$, $FeCl_3{\cdot}6H_2O$, Na_2SO_4, $NH_3{\cdot}H_2O$, $Na_2C_2O_4$, salicylic acid, benzoquinone, sodium acetate and ethanol were purchased from Sigma-Aldrich. All chemical reagents were of analytical grade and without any further purification.

Synthesis of α-Fe_2O_3/Bi_2WO_6 composites. Bi_2WO_6 was synthesized via the same method as reported in our previous work[15]. Layered α-Fe_2O_3/Bi_2WO_6 heterojunctions were synthesized by *in situ* growth method. Typically, 2 g Bi_2WO_6 was ultrasonic dispersed in 120 mL ethanol for 30 minutes. Then, appropriate amount of $FeCl_3{\cdot}6H_2O$ and sodium acetate were added into the above solution. After vigorous stirring for about 2 h, the mixture was transformed to a 200 mL Teflon-lined autoclave and then heated in an oven at 180 °C for 24 h. The obtained participates were collected by vacuum filtration and washed with deionized water and ethanol several times. Finally, these samples were dried in air at 70 °C before being used. Composites of 2, 4 and 6% α-Fe_2O_3/Bi_2WO_6 samples were prepared, respectively. Pure hexagonal nanoplates of α-Fe_2O_3 were synthesized without the addition of Bi_2WO_6 via the method reported in the reference[26].

Characterization of samples. The crystal phase and composition of these as-prepared catalysts were obtained using an X-ray diffraction (XRD, model D/max RA, Rigaku Co., Japan with Cu Kα radiation). Raman measurement was performed using a LABRAM-HR Ramas-cope fitted with a spectra physics argon ion laser. Laser radiation ($\lambda = 514$ nm) was used as excitation source at 20 mW. The surface properties were performed using X-ray photoelectron spectroscopy (XPS) measurement (Thermo, ESCALAB 250). The standard binding energy of 284.8 eV from C1s value was chosen as a reference. The morphology and microstructure information of the catalysts were obtained by Scanning electron microscopy (SEM, FEI-quanta 200F, USA) and transmission electron microscopy (TEM, H-600, Hitachi, Ltd., Japan). The specific surface area of catalysts was ascertained by using a nitrogen adsorption apparatus (Beijing JWGB Sci. & Tech. Co., Ltd). The light adsorption ability of

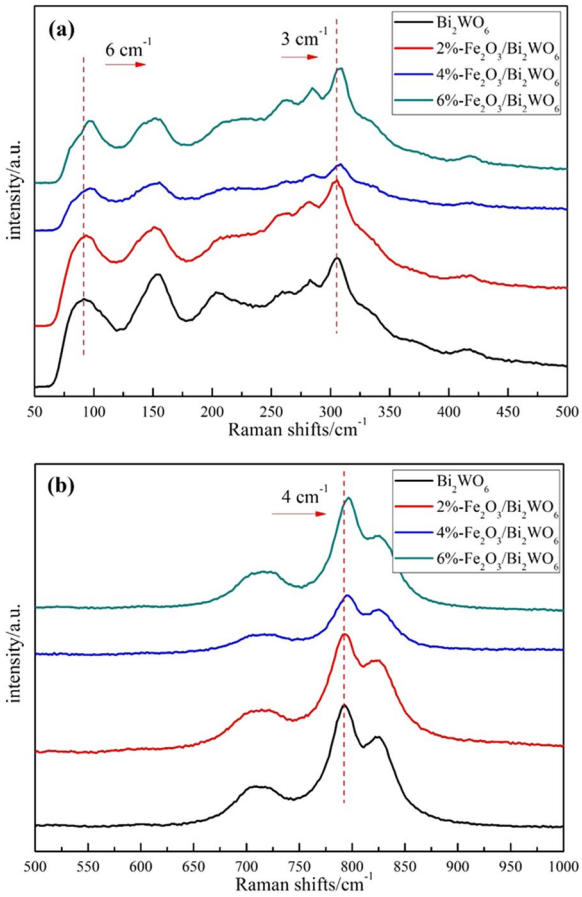

Figure 2. Raman spectra for pure Bi_2WO_6 and Fe_2O_3/Bi_2WO_6 composites in the range of (**a**) 50–500 cm^{-1} and (**b**) 500–1000 cm^{-1}.

these samples was obtained by using a Scan UV-visible spectrophotometer (UV-visible DRS: TU-1901, China) equipped with an integrating sphere assembly. The spectra were recorded at room temperature in air, ranging from 230 to 850 nm. Photoluminescence (PL) spectra and time-resolved photoluminescence (TRPL) spectra were recorded using a fluorospectrophotometer (PL: RAMANLOG 6, USA) with a 390 nm Ar^+ laser as excitation source. All these photoelectrochemical properties of the samples were measured on an electrochemical system (CHI 660B, Shanghai, China) using a three-electrode photo electrochemical cell. Platinum wire and saturated Ag/AgCl electrode were used as the counter electrode and the reference electrode, respectively. The working electrode was composed of indium tin oxide (ITO, 20 × 30 × 1.1 mm, 15 Ω) with an area of about 1 cm^2, glass coated with the prepared samples. The details of preparing working electrode was reported in our previous work[15]. The electrolyte was 0.2 M Na_2SO_4 solution. Electron spin resonance (ESR) signals of radical species trapped by 5, 5-dimethyl-1-pyrroline N-oxide (DMPO) were detected on a JES FA200 spectrometer.

Photocatalytic activity tests. Photocatalytic activity of as-prepared samples was evaluated via photodegradation of toluene. Experiment was performed in a 1.5 L batch reactor sealed with quartz plate. Circulating cooling water in the jacket around the reactor was used to control the reaction temperature. For each test, 0.1 g photocatalyst was uniformly dispersed onto a glass dish with a diameter about 10 cm. After that, the catalyst-coated dish was played on the bottom of the reactor. An appropriate amount of toluene was injected into the reactor with a micro-springe. Before each test, the system was maintained in the darkness to achieve adsorption-desorption equilibrium. The initial concentration of toluene was controlled at about 25 ppm. A 300 W Xe lamp (Celhx300UV, Ceaulight, China) equipped with two optical glass filters (420 nm $< \lambda <$ 780 nm) was used as the light source. At given intervals (every 30 minutes), the concentration of toluene in the reactor was measured with a GC-FID (FULI 9790, China). The schematic of the photocatalytic reactor was provided in the supporting information (see Fig. S1).

Results and Discussion

Structure and morphology. The crystal structure and phase composition of these samples were detected by XRD analysis (Fig. 1a). For pure Bi_2WO_6, distinct diffraction peaks at 28.5°, 32.8°, 47.1°, 55.7°, 58.5° and 75.8° were perfectly corresponding to (131), (200), (202), (133), (262) and (391) crystallographic planes (PDF#39-0256)[27], respectively. In addition, all the diffraction peaks of pure α-Fe_2O_3 (see Fig. S2) were in good agreement with those for hematite (PDF#33-0664)[28]. The intensity of the diffraction peaks of α-Fe_2O_3/Bi_2WO_6 composites was stronger than that of pure Bi_2WO_6 (see Fig. 1a), which could be ascribed to the growth of crystals during the

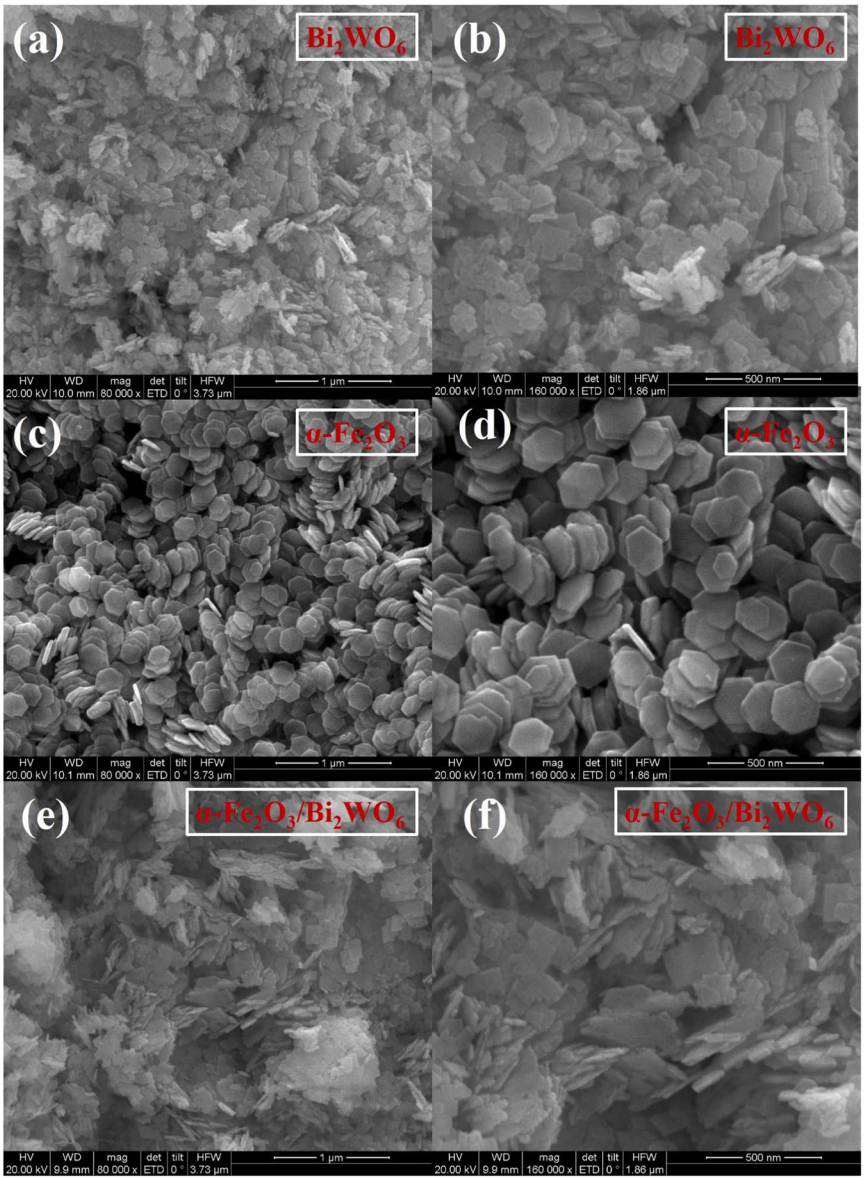

Figure 3. SEM images of (**a**,**b**) pure Bi_2WO_6, (**c**,**d**) pure α-Fe_2O_3 and (**e**,**f**) 4%-Fe_2O_3/Bi_2WO_6 composite.

hydrothermal process. It was noteworthy that no peaks of α-Fe_2O_3 were observed for α-Fe_2O_3/Bi_2WO_6 composite photocatalysts, which may be ascribed to the high dispersion and low content of α-Fe_2O_3[29]. Moreover, a shift to lower 2θ value of the band related to (131) lattice plane for α-Fe_2O_3/Bi_2WO_6 could be observed (Fig. 1b). Based on Bragg's law, this fact verified the slight expansion of the interplanar spacing related to Bi_2WO_6[30]. According to the reference[31], the increase in d spacing of Bi_2WO_6 could be attributed to the partial substitution of Bi sites by Fe ions. From this viewpoint, it was confirmed that there existed strong interaction between α-Fe_2O_3 and Bi_2WO_6. Similar results were also reported by the reference[25].

Raman spectra were also collected to further analyze the phase structure of photocatalysts. In Fig. 2, the peaks in the 60–160 cm^{-1}, 200–400 cm^{-1} and 600–1000 cm^{-1} regions could be assigned to translational motions of Bi^{3+} and W^{6+}, WO_6 bending modes and Bi-O stretching and bending modes, and W–O bands stretching modes[32], respectively. In detail, the bands at about 95 cm^{-1} and 305 cm^{-1} were associated with translational modes involving simultaneous motions of Bi^{3+} and WO_6[6–33]. The peak at about 710 cm^{-1} could be ascribed to an antisymmetric bridging mode of the tungstate chain[33,34]. Two bands at about 790 cm^{-1} and 820 cm^{-1} matched well with antisymmetric and symmetric A_g modes of terminal O–W–O groups[33,35]. No Raman vibrational peaks of α-Fe_2O_3 were detected, which may be due to a lower α-Fe_2O_3 loading[29]. As illustrated in Fig. 2a,b, three bands at 95 cm^{-1}, 305 cm^{-1} and 790 cm^{-1} of the α-Fe_2O_3/Bi_2WO_6 composites migrated to higher wave numbers, indicating the *in situ* growth of α-Fe_2O_3 on Bi_2WO_6 crystal had an influence on the phase structure of Bi_2WO_6. This finding fitted well with the results obtained from XRD characterization above.

The microstructure and morphology of the obtained samples were visualized by SEM, TEM and HR-TEM measurements. Figure 3 showed the SEM images of pure Bi_2WO_6, pure α-Fe_2O_3 and 4%-Fe_2O_3/Bi_2WO_6

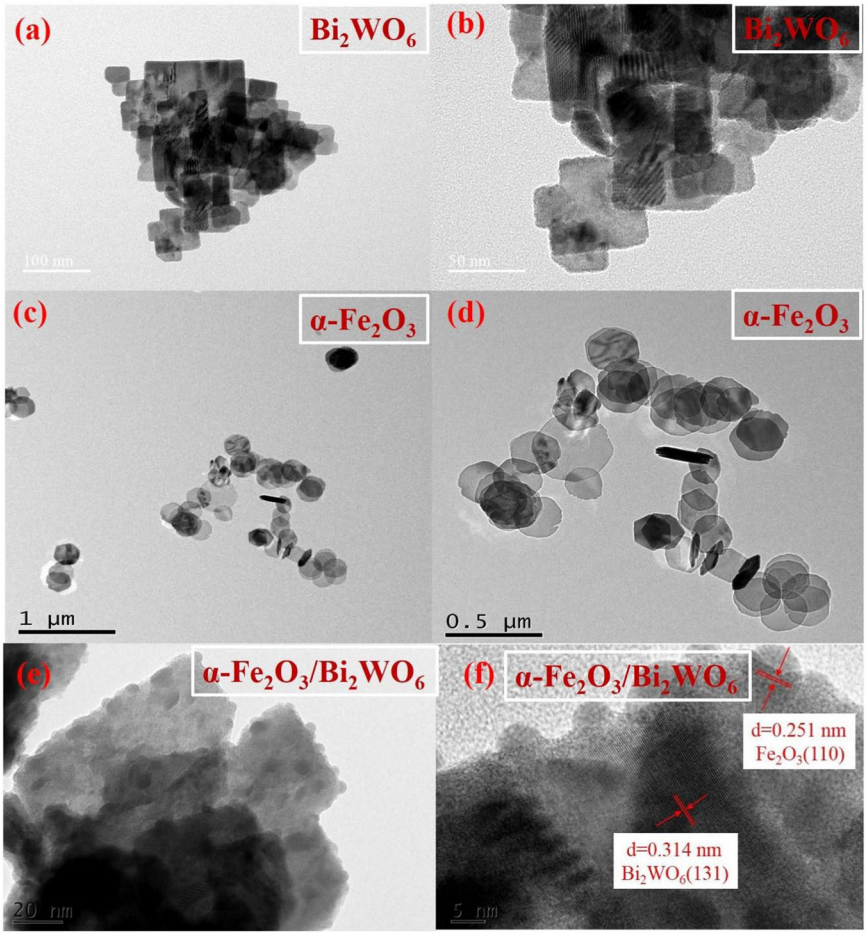

Figure 4. TEM images of pure (**a**,**b**) Bi_2WO_6, (**c**,**d**) pure α-Fe_2O_3, (**e**) TEM and (**f**) HR-TEM images of 4%-Fe_2O_3/Bi_2WO_6 composite.

composite, respectively. It could be clearly seen that the geometric shape of pure Bi_2WO_6 was a laminated structure (Fig. 3a,b). Pure α-Fe_2O_3 had a uniform and hexagonal nanoplate structure (Fig. 3c,d). No significant change could be observed in the SEM images of 4%-Fe_2O_3/Bi_2WO_6 composite (Fig. 3e,f) compared with that of pure Bi_2WO_6, indicating the prepared process hardly damaged the origin layered structure of pure Bi_2WO_6. Additionally, no hexagonal nanoplate structure of α-Fe_2O_3 could be found as well, which may be ascribed to the low content of α-Fe_2O_3[29]. The TEM images of pure Bi_2WO_6 (Fig. 4a,b) and pure α-Fe_2O_3 (Fig. 4c,d) showed layered structure as well. Figure 4e displayed that α-Fe_2O_3 nanosheets randomly grew on the laminated structure of Bi_2WO_6. A typical HR-TEM image of α-Fe_2O_3/Bi_2WO_6 composite was given in Fig. 4f. The lattice with interplanar distances of 0.314 nm and 0.251 nm attached to (131) lattice plane of Bi_2WO_6[30] and (110) lattice plane of Fe_2O_3[26], respectively. In view of long-time ultrasonication pretreatment in the TEM process, it could be concluded that there existed strong interlayer interaction between α-Fe_2O_3 and Bi_2WO_6 nanoplates[36].

Surface composition analysis. X-ray photoelectron spectroscopy (XPS) measurement was used to identify the oxidation state and surface composition of α-Fe_2O_3/Bi_2WO_6 composites. For pure Bi_2WO_6, two peaks with binding energy of 164.60 eV and 159.25 eV were the split signals of Bi 4f (Fig. 5a), which could be assigned to the Bi^{3+} species in the sample[37]. Two characteristic peaks in the W 4f spectrum (Fig. 5b) at 37.70 eV and 35.50 eV were ascribed to W $4f_{5/2}$ and W $4f_{7/2}$[37], respectively. As displayed in Fig. S3, the peaks at 724.58 eV and 710.68 eV belonged to Fe $2p_{1/2}$ and Fe$2p_{3/2}$[38], suggesting the presence of Fe^{3+}. The peaks of Bi^{3+} 4f and W^{6+} 4f both showed a slightly positive shift (see Fig. 5), which indicated the surface electron density for Bi and W had changed[39,40]. This result indicated that the heterostructure interface between Fe_2O_3 and Bi_2WO_6 could have been formed[15,36]. It agreed well with the abovementioned XRD, Raman and HR-TEM results.

Optical properties. Expanding the visible light absorption range played a crucial role for the modification of photocatalysts towards improving the visible-light photocatalytic activity. Optical diffuse reaction spectra (DRS) was used to estimate the visible light adsorption property of as-obtained photocatalysts. As shown in Fig. 6, pure α-Fe_2O_3 displayed an excellent light absorption ability among almost the whole visible light range due to its narrow band gap[41]. The spectrum of α-Fe_2O_3/Bi_2WO_6 composites showed obvious red-shift compared with pure

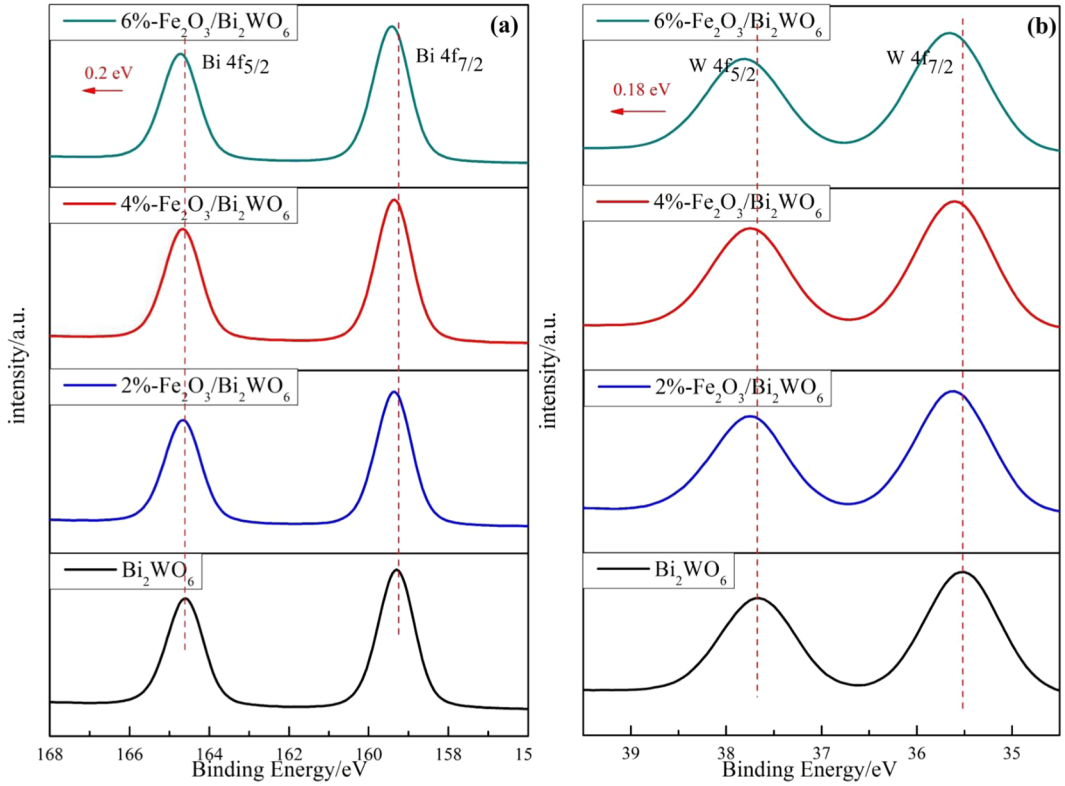

Figure 5. High-resolution XPS spectra of (**a**) Bi 4f (**b**) W 4f for different photocatalysts.

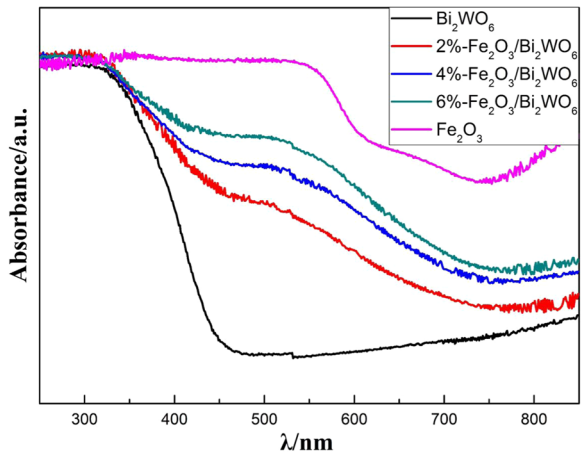

Figure 6. UV−vis absorption spectra of pure Bi_2WO_6, pure α-Fe_2O_3 and α-Fe_2O_3/Bi_2WO_6 composites.

Bi_2WO_6, implying the improvement of the utilization of visible light[42]. Furthermore, the band gap of pure Bi_2WO_6 and pure Fe_2O_3 was calculated based on Kubelka–Munk theory to be about 2.65 eV and 1.95 eV, respectively (see Fig. S4). These results agreed well with the references[43,44].

Photoelectrochemical performances. Electrochemical impedance spectroscopy (EIS) was applied to shed light on the interface charge separation and transfer efficiency of different photocatalysts under visible light irradiation. The arc radius of Fe_2O_3/Bi_2WO_6 composites was smaller than that of pure Bi_2WO_6 and Fe_2O_3(see Fig. 7a), revealing that the photoexcited eletrons could easily transfer across the interface and efficiently migrate to the surface due to the Fe_2O_3/Bi_2WO_6 layered heteojunction[39,45]. Especially, the 4%-Fe_2O_3/Bi_2WO_6 composite had the smallest arc radius, indicating it possessed the least electrons transfer resistance. Tafel analysis was performed to get a vivid view of the current density values of the photocatalysts investigated under visible light irradiation[46]. Generally, larger values of corrosion current density and anodic Tafel slope meant more photogenerated pairs and faster electron transfer rate[12], which benefitting the photocatalytic process. As displayed in Fig. 7b, 4%-Fe_2O_3/

Sample	τ_1/ns	A_1/%	τ_2/ns	A_2/%	χ^2	τ_{av}/ns
Bi_2WO_6	0.7402	63.41	3.5458	36.59	1.407	2.8005
4%-Fe_2O_3/Bi_2WO_6	1.2237	60.52	5.8734	39.48	1.186	4.7478

Table 1. Kinetic parameters of the emission Decay of different samples.

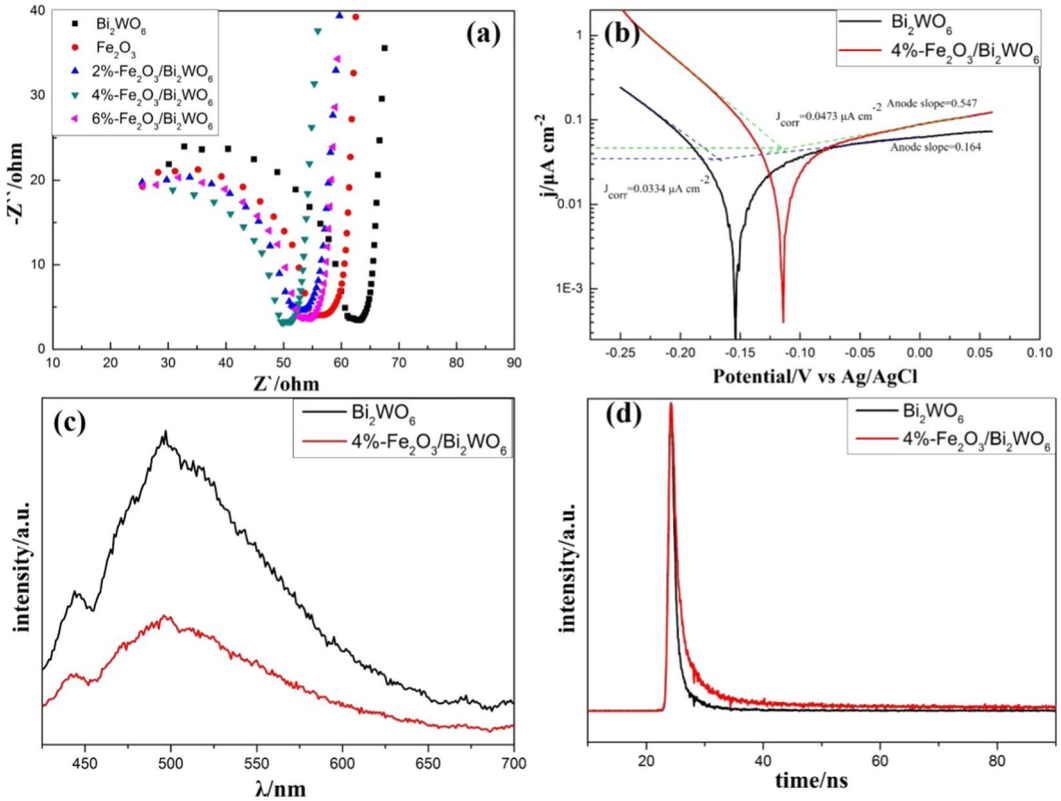

Figure 7. (**a**) Electrochemical impedance spectroscopy spectra of different catalysts, (**b**) Tafel polarization curves of the various electrodes under visible light irradiation, (**c**) Photoluminescence (PL) spectra and (**d**) time-resolved photoluminescence (TRPL) spectra of different samples.

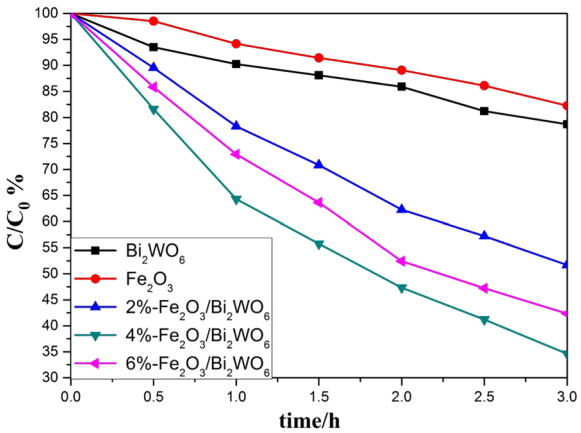

Figure 8. Photocatalytic degradation of gaseous toluene in the presence of different samples under visible light irradiation.

Bi_2WO_6 composite exhibited larger J_{corr} value and anodic slope as compared with pure Bi_2WO_6. Consequently, the results further demonstrated that the heterojunction between Fe_2O_3 and Bi_2WO_6 could improve charge transfer rate and efficiently separate photoexcited electrons and holes. Moreover, as shown in Fig. S5, the photocurrent of

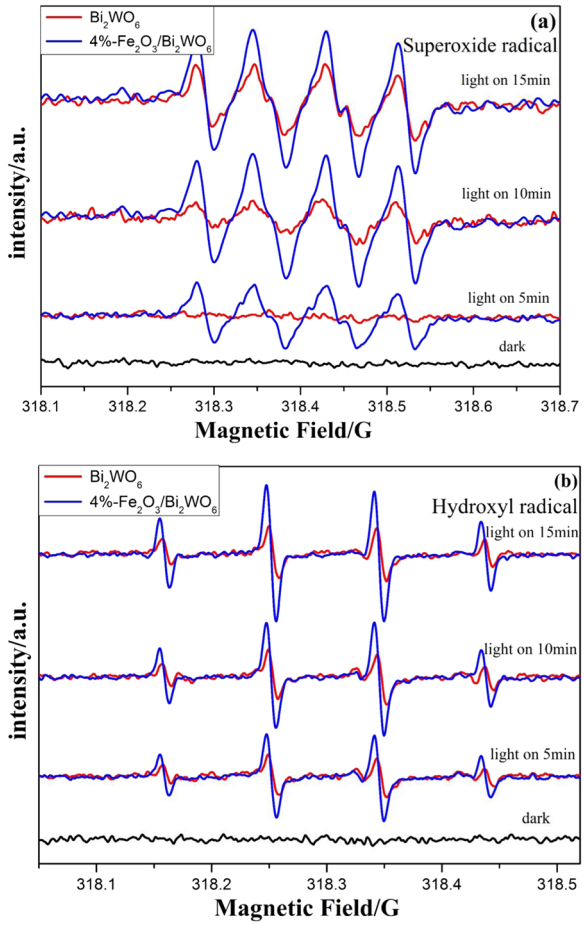

Figure 9. DMPO spin-trapping ESR spectra in Bi_2WO_6 and 4%-Fe_2O_3/Bi_2WO_6 composite in drak or under visible light irradiation: (**a**) in aqueous dispersion for DMPO-·O_2^- and (**b**) in methanol dispersion for DMPO-·OH.

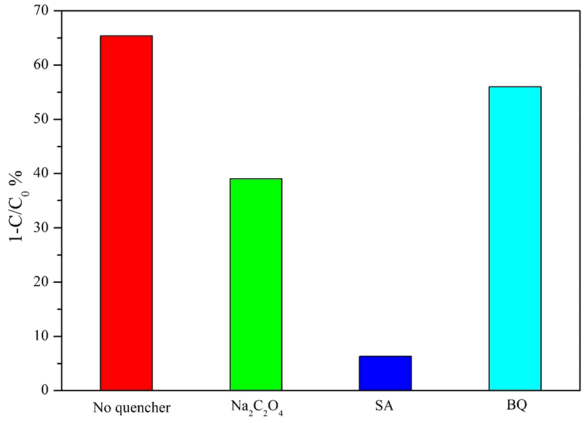

Figure 10. Photocatalytic activities of 4%-Fe_2O_3/Bi_2WO_6 composite for the photooxidation of toluene in the presence of different quenchers.

Fe_2O_3/Bi_2WO_6 composite was much higher than that of pure Bi_2WO_6, suggesting the separation ratio of photo-excited charges enhanced. Photoluminescence (PL) spectra was further used to demonstrate the recombination ratio of photoinduced pairs. As displayed in Fig. 7c, the intensity of 4%-Fe_2O_3/Bi_2WO_6 was much lower than that of pure Bi_2WO_6, indicating that the recombination of photogenerated charge carriers was effectively inhibited[15,47]. Time-resolved photoluminescence (TRPL) spectra (Fig. 7d) was also used to assess recombination kinetics of photoinduced electron-hole pairs. The TRPL decay spectrum waves were fitted by exponential decay kinetics function displayed as Eq. (1)[48]:

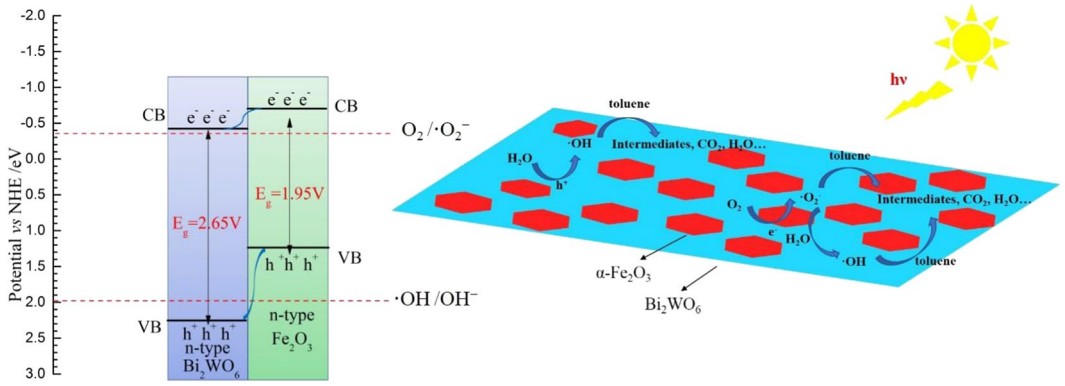

Figure 11. Diagram of the energy band levels of Fe_2O_3/Bi_2WO_6 composite and proposed possible photodegradation of toluene process.

$$I(t) = A_1 \exp(-t/\tau_1) + A_2 \exp(-t/\tau_2) \quad (1)$$

The average emission time was calculated based on Eq. (2) [48]:

$$\tau_{av} = \sum A_i \tau_i^2 / \sum A_i \tau_i \quad (2)$$

where τ_1 and τ_2 were lifetimes, A_1 and A_2 were the corresponding weighting factors. Based on the fitted results listed in Table 1, the average lifetime of 4%-Fe_2O_3/Bi_2WO_6 composite was longer than that of pure Bi_2WO_6, enhancing the likelihood of photoinduce pairs to participate in the reaction of gas-phase toluene photodegradation[39], thereby implying higher photocatalytic activity for Fe_2O_3/Bi_2WO_6 composites.

Photocatalytic performances. To evaluate the photocatalytic efficiency of as-prepared photocatalysts, gaseous toluene was chosen as a probe indoor air contaminant. The toluene degradation efficiency for the samples investigated was displayed in Fig. 8 and the relative apparent rate constant (k) based on pseudo-first-order kinetic model was obtained (see Fig. S6). Pure Bi_2WO_6 and α-Fe_2O_3 showed rather poor photocatalytic activity under three-hour visible light irradiation. In stark contrast, the gaseous toluene removal efficiency was remarkedly enhanced over Fe_2O_3/Bi_2WO_6 composites owing to their well photoelectrochemical property as discussed above. Among all the samples, 4%-Fe_2O_3/Bi_2WO_6 catalyst showed the highest photocatalytic activity, whose k value ($0.3469\,h^{-1}$) was much higher than those of pure Bi_2WO_6 ($0.0749\,h^{-1}$) and pure α-Fe_2O_3 ($0.0649\,h^{-1}$). Besides, the surface area didn't play an important role in enhancing the photocatalytic activity, as the surface area of 4%-Fe_2O_3/Bi_2WO_6 sample was modest (see Table S1). Based on the above analysis, it could be concluded that the layered heterojunctions between Fe_2O_3 and Bi_2WO_6 palyed a key role in promoting the photocatalytic process.

Possible photocatalytic mechanism. DMPO spin-trapping ESR technique was employed to verified the active radicals produced in the photocatalytic system. As presented in Fig. 9, no peaks could be observed in the darkness. Clearly, characteristic peaks for ·OH and $\cdot O_2^-$ emerged once the as-obtained samples were irradiated by visible light. Both intensity for ·OH and $\cdot O_2^-$ became stronger with increasing irradiation time. Notably, the 4%-Fe_2O_3/Bi_2WO_6 exhibited stronger intensity for ·OH and $\cdot O_2^-$ than that of pure Bi_2WO_6 under the same condition, implying the oxidation ability of the composite photocatalyst had been effectively promoted[49]. As reported in the references[50–52], the involvement of active radical species (such as $\cdot O_2^-$, ·OH and h^+) was very important in the photocatalytic process. Thus, free radicals trapping experiment was performed to further figure out the role of the radical species during the photocatalytic reaction. In a typical experiment, $Na_2C_2O_4$[53], salicylic acid (SA)[54] and benzoquinone (BQ)[55] were applied as scavengers of h^+, ·OH and $\cdot O_2^-$, respectively. As illustrated in Fig. 10, the addition of BQ had little effect on the photocatalytic activity. However, the toluene removal efficiency obviously decreased in the presence of $Na_2C_2O_4$ and SA. In particular, the degradation efficiency of toluene was whittled down into about 5% when adding appropriate amount of SA. Therefore, it could be inferred that h^+ and ·OH played dominant roles in the toluene photodegradation process.

Based on the Mott-Schottky analysis (see Fig. S7), the value of Fermi energy level was −0.30 eV and −0.60 eV (*vs* NHE) for Bi_2WO_6 and α-Fe_2O_3[56], respectively. For n-type semiconductor, the conduction band (CB) edge was more negative (about 0–0.2 eV) than Fermi level[57]. Herein, the difference value was set to 0.1 eV. Therefore, as illustrated in Fig. 11, the conduction band (CB) bottom and valence band (VB) top values of pure Bi_2WO_6 and pure α-Fe_2O_3 could be obtained. The *in situ* growth strategy could guarantee the intimate contact between Bi_2WO_6 and α-Fe_2O_3 with stronger interfacial interaction. Once the heterojunction was irradiated by visible light, both Bi_2WO_6 and α-Fe_2O_3 could generate electron-hole pairs. Due to the type-II heterojunction and intimate contact between Bi_2WO_6 and α-Fe_2O_3, the photoexcited electrons on the CB of α-Fe_2O_3 had the tendency to transfer to that of Bi_2WO_6, whereas photoinduced holes spontaneously moved to the VB of α-Fe_2O_3 (see Fig. 11). Therefore, the photogenerated electrons and holes could be separated efficiently, which greatly enhanced the photocatalytic activity. The CB bottom level of Bi_2WO_6 was more negative than that of $O_2/\cdot O_2^-$ (−0.33 eV)[58], thus

the photoexcited electrons could reduce oxygen molecules absorbed on the surface to $\cdot O_2^-$ species. What's more, part of O_2 could be reduced to H_2O_2 by photo-generated electrons based on the fact that the redox potential of O_2/H_2O_2 was 0.695 eV[59], then the formed H_2O_2 could produce ·OH by capture the photo-generated electrons[60,61]. Although the VB top value of α-Fe_2O_3 was less positive than the potential of $\cdot OH/OH^-$ (1.99 eV)[58], characteristic signals of ·OH (1:2:2:1 quartet pattern) could still be obviously observed in the ESR spectrum (see Fig. 9). This may be ascribed to the fact that part of the photogenerated holes remaining in the VB top of Bi_2WO_6 could also oxidize absorbed H_2O into ·OH. Similar phenomenon was also founded by Li. *et al.*[39]. Hence, these radical species had strong oxidation ability to destroy toluene molecule.

Conclusions

In summary, α-Fe_2O_3/Bi_2WO_6 layered heterojunctions were successfully synthesized via a simple *in situ* growth method in this work. XRD, Raman, HR-TEM and XPS results demonstrated there existed strong interaction between Bi_2WO_6 and α-Fe_2O_3. The α-Fe_2O_3/Bi_2WO_6 layered heterojunctions could effectively broaden visible light absorption range and improve photoexcited charges separation efficiency according to the characterization results of UV-vis, EIS, Tafel curve, PL and TRPL. Especially, 4%-Fe_2O_3/Bi_2WO_6 sample with strong interlayer interaction exhibited the highest photocatalytic activity. Given the results of ESR and trapping experiments, h^+ and ·OH species played a crucial role during the photocatalytic process of toluene removal. Such layered heterojunction photocatalyst had potential applications for indoor air purification.

References

1. Low, J., Yu, J., Jaroniec, M., Wageh, S. & Al-Ghamdi, A. A. Heterojunction photocatalysts. *Adv. Mater.* **29** (2017).
2. Zhou, P., Yu, J. & Jaroniec, M. All-solid-state Z-scheme photocatalytic systems. *Adv. Mater.* **26**, 4920–4935 (2014).
3. Zhang, L. & Jaroniec, M. Toward designing semiconductor-semiconductor heterojunctions for photocatalytic applications. *Appl. Surf. Sci.* **430**, 2–17 (2018).
4. Yu, H. *et al.* Three-in-one oxygen vacancies: whole visible-spectrum absorption, efficient charge separation, and surface site activation for robust CO_2 photoreduction. *Angew. Chem.* **58**, 3880–3884 (2019).
5. Chen, F. *et al.* Thickness-dependent facet junction control of layered $BiOIO_3$ single crystals for highly efficient CO_2 photoreduction. *Adv. Funct. Mater.* **28**, 1804284 (2018).
6. Yu, S. *et al.* Synchronously achieving plasmonic Bi metal deposition and I- doping by utilizing $BiOIO_3$ as the self-sacrificing template for high-performance multifunctional applications. *ACS Appl. Mater. Inter.* **7**, 27925–27933 (2015).
7. Garg, A. *et al.* Photocatalytic degradation of bisphenol-a using N, Co codoped TiO_2 catalyst under solar light. *Sci. Rep.* **9**, 765 (2019).
8. Qin, L., Wang, G. & Tan, Y. Plasmonic Pt nanoparticles-TiO_2 hierarchical nano-architecture as a visible light photocatalyst for water splitting. *Sci. Rep.* **8**, 16198 (2018).
9. Tang, Q. *et al.* Enhanced CO_2 photocatalytic reduction performance on alkali and alkaline earth metal ion-exchanged hydrogen titanate nanotubes. *Appl.Surf. Sci.* **463**, 456–462 (2019).
10. Neena, D. *et al.* Enhanced visible light photodegradation activity of RhB/MB from aqueous solution using nanosized novel Fe-Cd co-modified ZnO. *Sci. Rep.* **8**, 10691 (2018).
11. Peng, H., Liu, X., Tang, W. & Ma, R. Facile synthesis and characterization of ZnO nanoparticles grown on halloysite nanotubes for enhanced photocatalytic properties. *Sci. Rep.* **7**, 2250 (2017).
12. Zhao, W. *et al.* Synthesis, characterization, and photocatalytic properties of SnO_2/Rutile TiO_2/Anatase TiO_2 heterojunctions modified by Pt. *J. Phys. Chem. C.* **118**, 23117–23125 (2014).
13. Kong, J., Rui, Z. & Ji, H. Enhanced photocatalytic mineralization of gaseous toluene over $SrTiO_3$ by surface hydroxylation. *Ind. Eng. Chem. Res.* **55**, 11923–11930 (2016).
14. Wetchakun, N. *et al.* $BiVO_4/CeO_2$ nanocomposites with high visible-light-induced photocatalytic activity. *ACS Appl. Mater. Inter.* **4**, 3718–3723 (2012).
15. Xie, T., Liu, Y., Wang, H. & Wu, Z. Layered $MoSe_2/Bi_2WO_6$ composite with P-N heterojunctions as a promising visible-light induced photocatalyst. *Appl.Surf. Sci.* **444**, 320–329 (2018).
16. Huang, H. *et al.* Single-unit-cell layer established Bi_2WO_6 3D hierarchical architectures: Efficient adsorption, photocatalysis and dye-sensitized photoelectrochemical performance. *Appl. Catal. B: Environ.* **219**, 526–537 (2017).
17. He, W. *et al.* Activation of amorphous Bi_2WO_6 with synchronous Bi metal and Bi_2O_3 coupling: Photocatalysis mechanism and reaction pathway. *Appl. Catal. B: Environ.* **232**, 340–347 (2018).
18. Lv, Y., Yao, W., Zong, R. & Zhu, Y. Fabrication of wide–range–visible photocatalyst Bi_2WO_{6-x} nanoplates via surface oxygen vacancies. *Sci. Rep.* **6**, 1–9 (2016).
19. Wang, F. *et al.* Facile fabrication of direct Z-scheme MoS_2/Bi_2WO_6 heterojunction photocatalyst with superior photocatalytic performance under visible light irradiation. *J. Photoch. Photobio. A.* **335**, 140–148 (2017).
20. Mao, M. *et al.* Designing all-solid-state Z-Scheme 2D g-C_3N_4/Bi_2WO_6 for improved photocatalysis and photocatalytic mechanism insight. Green *Energy Environ* (2017).
21. Zhong, S., Lv, C., Zou, S., Zhang, F. & Zhang, S. Preparation of pumice-loaded CeO_2/Bi_2WO_6 photocatalysts and treatment of tetracycline wastewater with a continuous flow photocatalytic reactor. *J. Mater. Sci-Mater. El.* **29**, 2447–2454 (2017).
22. Meng, X. & Zhang, Z. Facile synthesis of BiOBr/Bi_2WO_6 heterojunction semiconductors with high visible-light-driven photocatalytic activity. *J. Photoch. Photobio. A.* **310**, 33–44 (2015).
23. Zhang, Z., Huang, J., Zhang, M., Yuan, Q. & Dong, B. Ultrathin hexagonal SnS_2 nanosheets coupled with g-C_3N_4 nanosheets as 2D/2D heterojunction photocatalysts toward high photocatalytic activity. *Appl. Catal. B: Environ.* **163**, 298–305 (2015).
24. Wang, J. *et al.* Atomic scale g-C_3N_4/Bi_2WO_6 2D/2D heterojunction with enhanced photocatalytic degradation of ibuprofen under visible light irradiation. *Appl. Catal. B: Environ.* **209**, 285–294 (2017).
25. Cheng, H., Hou, J., Takeda, O., Guo, X.-M. & Zhu, H. A unique Z-scheme 2D/2D nanosheet heterojunction design to harness charge transfer for photocatalysis. *J. Mater. Chem. A.* **3**, 11006–11013 (2015).
26. Han, S. *et al.* One-Step Hydrothermal synthesis of 2D hexagonal nanoplates of α-Fe_2O_3/Graphene composites with enhanced photocatalytic activity. *Adv. Funct. Mater.* **24**, 5719–5727 (2014).
27. Xu, P. *et al.* Preparation of TiO_2/Bi_2WO_6 nanostructured heterojunctions on carbon fibers as a weaveable visible-light photocatalyst/photoelectrode. Environ. *Sci-Nano.* **5**, 327–337 (2018).
28. Shi, Y., Li, H., Wang, L., Shen, W. & Chen, H. Novel alpha-Fe_2O_3/CdS cornlike nanorods with enhanced photocatalytic performance. *ACS Appl. Mater. Inter.* **4**, 4800–4806 (2012).
29. Zhang, K. *et al.* Fe_2O_3/3DOM $BiVO_4$: High-performance photocatalysts for the visible light-driven degradation of 4-nitrophenol. *Appl. Catal. B: Environ.* **202**, 569–579 (2017).
30. Huang, H. *et al.* Ce and F comodification on the crystal structure and enhanced photocatalytic activity of Bi_2WO_6 photocatalyst under visible light irradiation. *J. Phys. Chem. C.* **118**, 14379–14387 (2014).

31. Guo, S., Li, X., Wang, H., Dong, F. & Wu, Z. Fe-ions modified mesoporous Bi_2WO_6 nanosheets with high visible light photocatalytic activity. *J. Colloid. Interf. Sci.* **369**, 373–380 (2012).
32. Maczka, M. *et al*. Phonon-instability-driven phase transitions in ferroelectric Bi_2WO_6: Eu^{3+}: High-pressure Raman and photoluminescence studies. *Phys. Rev. B*. **77** (2008).
33. Zhang, L.-W., Wang, Y.-J., Cheng, H.-Y., Yao, W.-Q. & Zhu, Y.-F. Synthesis of porous Bi_2WO_6 thin films as efficient visible-light-active photocatalysts. *Adv. Mate.* **21**, 1286–1290 (2009).
34. Liu, Y., Wei, B., Xu, L., Gao, H. & Zhang, M. Generation of oxygen vacancy and OH radicals: a comparative study of Bi_2WO_6 and Bi_2WO_{6-x} nanoplates. *ChemCatChem* **7**, 4076–4084 (2015).
35. Obregón, S. & Colón, G. Erbium doped TiO_2–Bi_2WO_6 heterostructure with improved photocatalytic activity under sun-like irradiation. *Appl. Catal. B: Environ.* **140–141**, 299–305 (2013).
36. Xu, Q., Zhu, B., Jiang, C., Cheng, B. & Yu, J. Constructing 2D/2D Fe_2O_3/g-C_3N_4 direct Z-scheme photocatalysts with enhanced H_2 generation performance. *Solar RRL* **2**, 1800006 (2018).
37. Wu, R., Song, H., Luo, N. & Ji, G. Hydrothermal preparation of 3D flower-like $BiPO_4$/Bi_2WO_6 microsphere with enhanced visible-light photocatalytic activity. *J. Colloid. Interf. Sci.* **524**, 350–359 (2018).
38. Cao, K. *et al*. 3D Hierarchical porous α- Fe_2O_3 nanosheets for high-performance lithium-ion batteries. *Adv. Energy Mater.* **5**, 1401421 (2015).
39. Zhu, L. *et al*. Synthesis of the 0D/3D CuO/ZnO Heterojunction with enhanced photocatalytic activity. *J. Phys. Chem. C.* **122**, 9531–9539 (2018).
40. Huang, Y. *et al*. Synthesis of a $Bi_2O_2CO_3$/$ZnFe_2O_4$ heterojunction with enhanced photocatalytic activity for visible light irradiation-induced NO removal. *Appl. Catal. B: Environ.* **234**, 70–78 (2018).
41. Han, M. *et al*. Z-Scheme in a $Co_3(PO_4)_2$/α- Fe_2O_3 photocatalysis system for overall water splitting under visible light. *Catal. Sci. Technol.* **8**, 840–846 (2018).
42. Zhang, J. *et al*. Constructing two-dimension MoS_2/Bi_2WO_6 core-shell heterostructure as carriers transfer channel for enhancing photocatalytic activity. *Mater. Res. Bull.* **85**, 140–146 (2017).
43. Meng, X., Li, Z., Zeng, H., Chen, J. & Zhang, Z. MoS_2 quantum dots-interspersed Bi_2WO_6 heterostructures for visible light-induced detoxification and disinfection. *Appl. Catal. B: Environ.* **210**, 160–172 (2017).
44. Li, S., Hu, S., Zhang, J., Jiang, W. & Liu, J. Facile synthesis of Fe_2O_3 nanoparticles anchored on Bi_2WO_6 microflowers with improved visible light photocatalytic activity. *J. Colloid Interf. Sci.* **497**, 93–101 (2017).
45. Xie, T. *et al*. Synthesis of Bi-deficient monolayered Bi_2WO_6 nanosheets with enhanced photocatalytic activity under visible light irradiation. *Catal. Sci. Technol.* **9**, 1178–1188 (2019).
46. Zhao, W., Wang, Y., Yang, Y., Tang, J. & Yang, Y. Carbon spheres supported visible-light-driven CuO-$BiVO_4$ heterojunction: Preparation, characterization, and photocatalytic properties. *Appl. Catal. B: Environ.* **115–116**, 90–99 (2012).
47. Luo, S. *et al*. $CuInS_2$ quantum dots embedded in Bi_2WO_6 nanoflowers for enhanced visible light photocatalytic removal of contaminants. *Appl. Catal. B: Environ.* **221**, 215–222 (2018).
48. Ge, M. Z. *et al*. *In situ* plasmonic Ag nanoparticle anchored TiO_2 nanotube arrays as visible-light-driven photocatalysts for enhanced water splitting. *Nanoscale.* **8**, 5226–5234 (2016).
49. Wang, J. *et al*. 0D/2D interface engineering of carbon quantum dots modified Bi_2WO_6 ultrathin nanosheets with enhanced photoactivity for full spectrum light utilization and mechanism insight. *Appl. Catal. B: Environ.* **222**, 115–123 (2018).
50. Huang, H. *et al*. Macroscopic polarization enhancement promoting photo- and piezoelectric-induced charge separation and molecular oxygen activation. *Angew. Chem.* **56**, 11860–11864 (2017).
51. Huang, H. *et al*. Anionic group self-doping as a promising strategy: band-gap engineering and multi-functional applications of high-performance CO_3^{2-}-doped $Bi_2O_2CO_3$. *ACS Catal.* **5**, 4094–4103 (2015).
52. Chen, F., Huang, H., Guo, L., Zhang, Y. & Ma, T. The role of polarization in photocatalysis. *Angew. Chem. Int. Ed* (2019).
53. Liu, Z. *et al*. One-pot sequential synthesis of magnetically separable Fe_3O_4/AgCl photocatalysts with enhanced activity and stability. *Russ. J. Phys.Chem. A.* **91**, 500–510 (2017).
54. Cheng, T.-C., Yao, K.-S., Hsieh, Y.-H., Hsieh, L.-L. & Chang, C.-Y. Optimizing preparation of the TiO_2 thin film reactor using the Taguchi method. *Mater. Design.* **31**, 1749–1751 (2010).
55. Huang, H. *et al*. *In situ* assembly of BiOI@$Bi_{12}O_{17}C_{l2}$ p-n junction: charge induced unique front-lateral surfaces coupling heterostructure with high exposure of BiOI {001} active facets for robust and nonselective photocatalysis. *Appl. Catal. B: Environ.* **199**, 75–86 (2016).
56. Kanan, M. W. & Nocera, D. G. *In situ* formation of an oxygen-evolving catalyst in neutral water containing phosphate and Co^{2+}. *Science.* **321**, 1072–1075 (2008).
57. Wang, Y. *et al*. One-step hydrothermal synthesis of a novel 3D $BiFeWO_x$/Bi_2WO_6 composite with superior visible-light photocatalytic activity. *Green Chem* (2018).
58. Zhao, X. *et al*. Biomass carbon modified Z-scheme g-C_3N_4/Co_3O_4 heterojunction with enhanced visible-light photocatalytic activity. *Catal. Commun.* **112**, 49–52 (2018).
59. Dong, F. *et al*. An Advanced semimetal-organic Bi spheres-g-C_3N_4 nanohybrid with spr-enhanced visible-light photocatalytic performance for NO purification. *Environ. Sci. Technol.* **49**, 12432–12440 (2015).
60. Sun, Y., Zhao, Z., Dong, F. & Zhang, W. Mechanism of visible light photocatalytic NO_x oxidation with plasmonic Bi cocatalyst-enhanced $(BiO)_2CO_3$ hierarchical microspheres. *Phys. Chem. Chem. Phys.* **17**, 10383–10390 (2015).
61. Shi, Q. *et al*. Enhanced visible-light driven photocatalytic mineralization of indoor toluene via a $BiVO_4$/reduced graphene oxide/Bi_2O_3 all-solid-state Z-scheme system. *J. Alloy. Compd.* **662**, 108–117 (2016).

Acknowledgements

This research is financially supported by the National Key Research and Development Program of China (2017YFC0210201), the Program for Zhejiang Leading Team of S&T Innovation (Grant No. 2013TD07).

Author Contributions

Taiping Xie designed, performed most of the experiments and wrote the manuscript. Yue Liu, Haiqing Wang and Zhongbiao Wu supervised the research work. All authors were contributed to discussion and writing the manuscript.

Additional Information

Supplementary information accompanies this paper at https://doi.org/10.1038/s41598-019-43917-w.

Competing Interests: The authors declare no competing interests.